NANO LETTERS

Letter

pubs.acs.org/NanoLett

Conformal Fe_3O_4 Sheath on Aligned Carbon Nanotube Scaffolds as High-Performance Anodes for Lithium Ion Batteries

Yang Wu, Yang Wei, Jiaping Wang,* Kaili Jiang, and Shoushan Fan

Department of Physics and Tsinghua-Foxconn Nanotechnology Research Center, Tsinghua University, Beijing, 100084, People's Republic of China

Supporting Information

ABSTRACT: A uniform Fe_3O_4 sheath is magnetron sputtered onto aligned carbon nanotube (CNT) scaffolds that are directly drawn from CNT arrays. The Fe_3O_4–CNT composite electrode, with the size of Fe_3O_4 confined to 5–7 nm, exhibits a high reversible capacity over 800 mAh g^{-1} based on the total electrode mass, remarkable capacity retention, as well as high rate capability. The excellent performance is attributable to the superior electrical conductivity of CNTs, the uniform loading of Fe_3O_4 sheath, and the structural retention of the composite anode on cycling. As Fe_3O_4 is inexpensive and environmentally friendly, and the synthesis of Fe_3O_4–CNT is free of chemical wastes, this composite anode material holds considerable promise for high-performance lithium ion batteries.

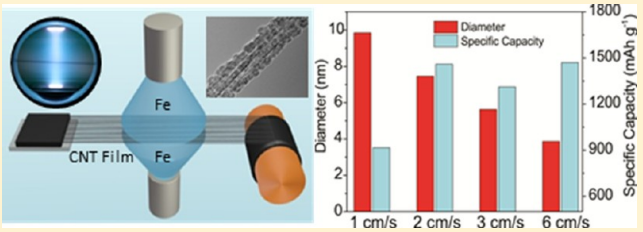

KEYWORDS: *Iron oxide, carbon nanotube, anode, magnetron sputtering, lithium ion battery*

Materials for electrodes of lithium ion batteries (LIBs) have been intensely explored due to the demand of renewable energy sources for a wide spectrum of applications, from portable electronics to electrical vehicles (EVs).[1−4] To this end, LIBs available in the market use graphite as the anode material.[5,6] Practical graphite anodes exhibit theoretical lithium storage capacities of around 370 mAh g^{-1} with an end compound of LiC_6 in terms of an intercalation mechanism.[6] Efforts to exceed this value have been a pivot in the research of anode materials. As a matter of fact, other potential candidates such as Si,[7,8] Sn,[9,10] tin-based alloys,[11,12] and metal oxides[13,14] with superior capacities have been considered for the next generation of LIBs. Among these materials, Fe_3O_4 is low-cost, biocompatible, and environmentally friendly.[15,16] The problem of Fe_3O_4 is its poor conductivity, which results in rapid capacity fading and poor calendar life. Nanostructured Fe_3O_4 with carbon coating[17,18] or nanosized metal current collectors[19,20] has displayed high capacities close to its theoretical value of 924 mAh g^{-1} via a conversion reaction. Another solution is to introduce conductive agents such as carbon nanofibers, graphene, and carbon nanotubes (CNTs) to make composite electrodes, which demonstrated both high capacity and good capacity retention.[21−24] Using CNT as a lithium storage material is yet satisfactory because the graphene layers in CNTs are closed so that the insertion of a lithium ion is energetically forbidden even for a single-walled CNT.[25,26] However, the expectation to turn CNTs into conductive additives and mechanical supports for novel anode materials has been nourished in light of their high aspect ratios and proved superior mechanical and electrical properties.

The challenge of making Fe_3O_4–CNT composite was the synthesis and the precise control on dimensions of nanoparticles.[27] Most of successful synthesis was based on the wet chemistry, where a strong dependence on reaction conditions was required and chemical wastes were inevitably generated. Nanomaterials can also be fabricated via dry methods such as magnetron sputtering. With this method, uniform deposition of nanosized carbides, nitrides, and oxides with low dimensionality on a variety of substrates was reported.[28,29] However, attempts of conformal coating on CNTs were always prohibited by the small pore sizes of the CNT matrix. Instead, nanoflakes were formed on the top of the CNT array substrate.[30] To tackle this issue, Au nanoparticles could be initially sputtered into a room temperature ionic liquid and then self-assembled onto already dispersed CNTs.[31] Although a narrow size distribution was obtained, the problems remained as the low loading of nanoparticles and inevitable dependence of expensive ionic liquids.

To develop magnetron sputtering as a synthetic methodology for Fe_3O_4–CNT nanocomposite, the key issue is how to completely disperse CNTs from dense CNT arrays or mats into a self-sustained nanostructure. Indeed, drawing CNT films from superaligned CNT (SACNT) arrays is considered as one of the best approaches. Such SACNT films are composed of only one layer of parallel CNTs, formed as a result of end-to-end joining of CNT bundles.[32,33] Previously, we have demonstrated that SACNT films can be assembled in a cross-stacked fashion and then exploited as conductive agents for SnO_2[34] or as current collectors[35] for graphite anodes to demonstrate remarkable improvements in the battery performance. In this work, a single layer of the SACNT film was introduced into the magnetron

Received: December 17, 2012
Published: January 8, 2013

sputtering chamber to allow the controllable growth of Fe_3O_4 via a spontaneous oxidation step. This attempt explicitly resulted in a core−sheath structure as a consequence of the conformal deposition of Fe_3O_4 nanoparticles on the SACNT film. In this approach, the ordered SACNT films drawn from SACNT arrays possess three important functions. First, the SACNT film is composed of segregated and aligned CNTs. A single layer SACNT film can be regarded as an ideal structure to achieve a homogeneous coating by magnetron sputtering since each CNT is exposed. Second, the superior mechanical property renders SACNTs as an excellent flexible scaffold to host and confine Fe_3O_4 nanoparticles and thus avoid the agglomeration of nanoparticles caused by the volumetric change in the electrochemical reaction. Third, SACNTs can also be utilized as a conducting additive and serve as a current collector to improve the poor conductivity of nano-Fe_3O_4. Therefore, the Fe_3O_4−SACNT composite fabricated by a one-step DC magnetron sputtering is expected as a promising anode material for LIBs with excellent reversible capacity, cyclic stability, and rate capability.

The successful integration of CNT drawing and magnetron sputtering was implemented in a lab-designed apparatus as shown in Figure 1a. SACNT arrays on Si substrates were fixed on one end of the sputtering chamber. The sputtering was carried out in Ar atmosphere. The chamber was first evacuated to a dynamic vacuum of 2×10^{-3} Pa for 15 min. Then Ar was backfilled to 1 Pa. The SACNT film was pulled through two opposite magnetron sputtering guns with Fe targets at a separation of ca. 15 cm (Figure 1b). The magnetron sputtering was performed at 50 W (500 V and 100 mA). At the other end of the chamber, the SACNT film was rolled on a Cu cylinder (Figure 1c). The sample was then shrunk with ethanol and taken off from the Cu cylinder. Due to the mechanical strength of CNTs, the sample was self-sustained and can be arranged into any sizes for further characterization. A typical photograph of a 200-layer SACNT film after the deposition was shown in Figure 1d. No further processes were applied. We note that all parameters except for the spinning speed of the Cu cylinder were fixed during the sample preparation step. The deposition started as the SACNT film entered the region of sputtered plasma and stopped as soon as the film was drawn out. Therefore, the speed of film drawing was the only variable to adjust the thickness of the deposit. Hence, we arranged all samples into four categories, Fe_3O_4−SACNT-1, Fe_3O_4−SACNT-2, Fe_3O_4−SACNT-3, and Fe_3O_4−SACNT-6, where the Arabic number denoted the drawing speed of films in cm s^{-1}.

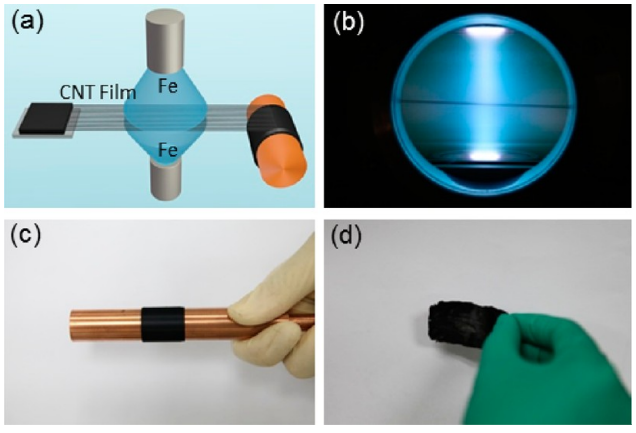

Figure 1. (a) Schematic illustration of the sputtering synthesis of Fe_3O_4−SACNT composites. (b) A photograph taken in the magnetron sputtering process. The black line in the middle indicates the CNT film. (c) A photograph of the Cu cylinder wrapped with CNTs after sputtering. (d) A photograph of a free-standing Fe_3O_4−SACNT sample peeled off from the Cu cylinder.

The formation of iron oxides might be due to the spontaneous oxidation in the sputtering step. The reactive sputtering method has been widely adopted to grow Fe_3O_4 film on SiO_2 substrates for magnetic applications.[36] Unlike established reactive sputtering methods, we did not intentionally introduce the O_2 into the reactor, but took advantage of the oxygen impurity. In this work, this strategy directly led to the formation of iron oxides. As shown in Figure 2a, Fe_3O_4 was identified as the major phase as almost all reflection peaks on the X-ray diffraction (XRD) pattern agreed well with the theoretical peak positions (magnetite, space group $Fd\bar{3}m$, a = 0.8396 nm).[37] The only exception occurs at ca. 26°, corresponding to the reflection by the adjacent graphene layers of CNTs. The analysis of X-ray photoelectron spectroscopy (XPS) confirmed oxidation states of Fe (Figure 2b). The peak position of Fe $2p_{3/2}$ at 711 eV corresponded to iron oxides.[38] Importantly, the absence of any XPS component at 707 eV, corresponding to elementary Fe, indicated the complete oxidation of Fe. Indeed, on a variety of bulk metals, the exposure to oxygen always led to an oxide layer of several

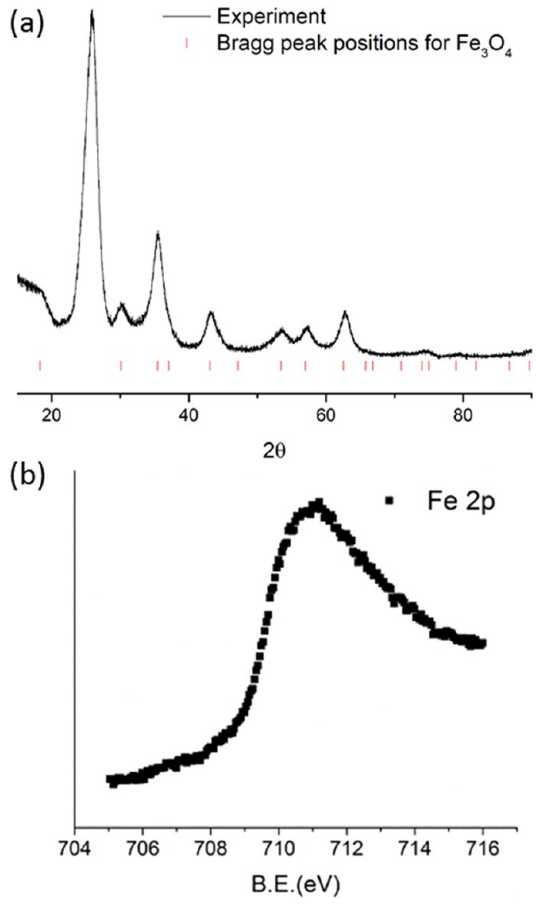

Figure 2. (a) An XRD pattern of Fe_3O_4−SACNT. Red lines are calculated peak positions according to the crystal structure information of Fe_3O_4. (b) Plot of a narrow scan of the Fe $2p_{3/2}$ XPS spectrum.

dx.doi.org/10.1021/nl3046409 | Nano Lett. 2013, 13, 818−823

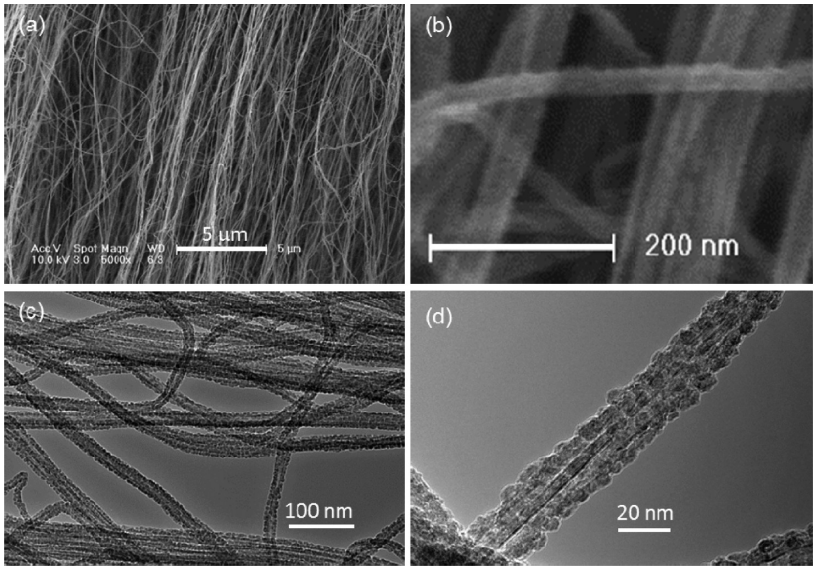

Figure 3. SEM images in (a) low magnification and (b) high magnification, and TEM images in (c) low magnification and (d) high magnification for the precycle Fe_3O_4–CNT composite anode.

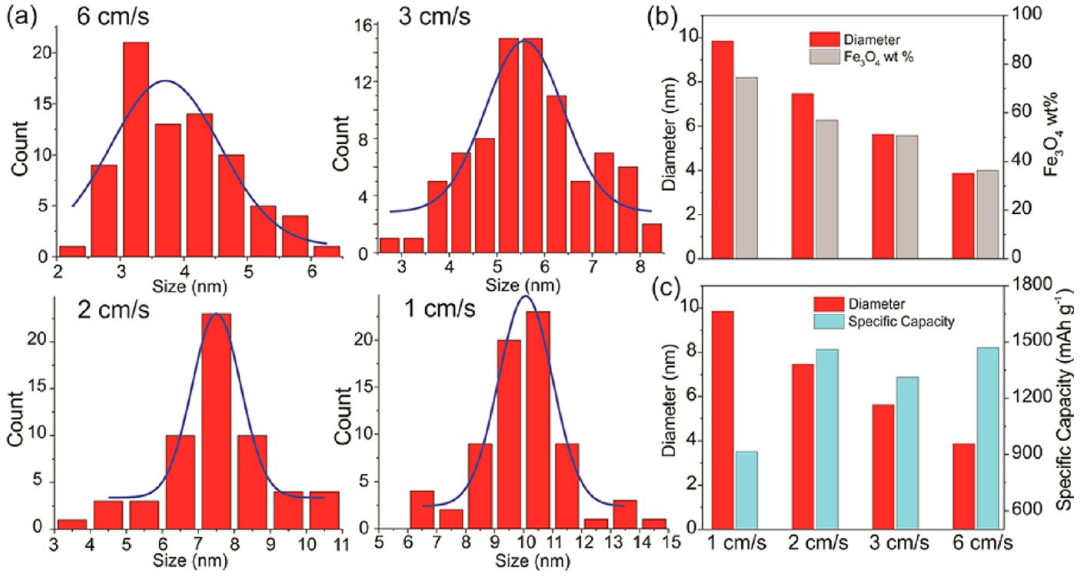

Figure 4. (a) Statistical size distributions of Fe_3O_4 particles deposited on CNTs at different film drawing speeds. Note that the size distribution becomes narrower as the speed decreases. (b) Comparison between the average particle diameter and the mass fraction of Fe_3O_4. (c) Comparison between the average particle diameter and the discharge capacity at 20th cycle, at different CNT film drawing speeds.

nanometers thick. In this sense, even if there were unreacted sputtered Fe clusters with sizes comparable to the thickness of the oxide layer, they would be oxidized completely as soon as we opened the sputtering chamber. Thus, this one-step and liquid-free procedure was effective to make Fe_3O_4–SACNT composites, and no postannealing process was required.

The microstructures of such composites were analyzed with scanning electron microscopy (SEM) and transmission electron microscopy (TEM). Figure 3a showed an SEM image of the top surface of a rolled 200-layer Fe_3O_4–SACNT-2 film after the deposition. Almost all SACNTs were aligned. There were also curved SACNTs in the sample. We note that this kind of SACNTs will bridge those paralleled ones and facilitate the electron transfer between layers. The diameter of the SACNT bundles can be estimated as around 30 nm from high magnification SEM images, in which the rough surface, corresponding to the Fe_3O_4 deposition, was also appreciable (Figure 3b). The variation in the diameter can be attributed to the number of SACNTs in each of SACNT bundles. As an ordered scaffold, the SACNT film not only hosted Fe_3O_4 nanoparticles but also regulated their growth. Note that the Fe_3O_4 coating only occurred on CNTs, leaving spaces between SACNTs still available. These pores as shown in the SEM images will enable the easy electrolyte infiltration. The analysis of TEM images revealed that the Fe_3O_4 sheath was actually composed of discrete Fe_3O_4 nanoparticles with diameters less than 10 nm, which orderly arranged along each of SACNTs (Figure 3c,d). Only Fe, O, and C were found in the element analysis (Figure S1). The TEM image clearly demonstrated the complete dispersion of Fe_3O_4. The Fe_3O_4 sheath only consisted of one layer of Fe_3O_4 nanoparticles, suggesting the preferential growth on the SACNTs. In comparison with a typical TEM

dx.doi.org/10.1021/nl3046409 | Nano Lett. 2013, 13, 818–823

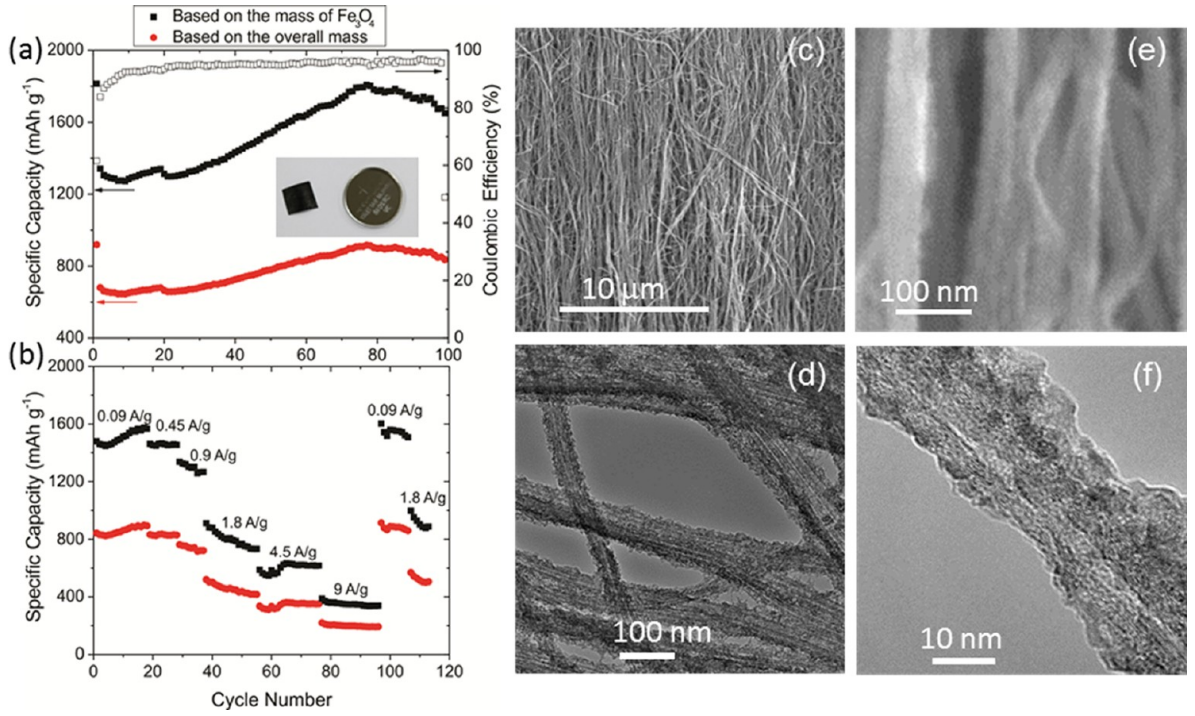

Figure 5. (a) Reversible specific capacity and (b) rate capability of Fe_3O_4–SACNT. Values based on the Fe_3O_4 mass and the total anode mass are in black and red colors, respectively. The empty black square in a illustrates the Coulombic efficiency. Inset in a: photograph of a Fe_3O_4–SACNT electrode before sealed in a CR 2016 cell. (c and d) Postcycle SEM and TEM images. (e and f) Corresponding SEM and TEM images in high magnifications, respectively.

image of a pristine SACNT (Figure S2), we only observed little structural damage on the graphene layer of SACNT after the sputtering process, indicating that the integrity of SACNT was preserved. The diameters of Fe_3O_4 particles were statistically analyzed from the TEM images (Figure 4a). It turned out that the average diameter and Fe_3O_4 wt % were a function of the speed of film drawing. Both the average size and the mass fraction of Fe_3O_4 increased as the speed of CNT drawing decreased. For example, the Fe_3O_4–SACNT-1 samples possessed the largest average diameter of Fe_3O_4 of 10.8 nm and a corresponding mass fraction of 74%, while the Fe_3O_4–SACNT-6 samples showed the smallest diameter of 3.6 nm and a mass fraction of 38% (Figure 4b). The size distribution of Fe_3O_4 also became narrower with slower CNT drawing speeds, suggesting the growth of Fe_3O_4 was more homogeneous. Therefore, we conclude so far that this magnetron sputtering method has led to a conformal and controllable coating of Fe_3O_4 on the CNT scaffold. In the Fe_3O_4–SACNT composite, it is rational to expect that the continuous SACNTs will behave as an ideal conductor to promote the electron transfer.

As the lithium storage of Fe_3O_4 is accounted for by the conversion reaction mechanism, the actual capacity and reversibility would be affected by the size and the morphology of the material. The galvanostatic tests in a voltage window of 0.1–3 V were performed in a 2016 coin-cell arrangement where Li foils were always used as counter electrodes. Twenty conditioning cycles at a current density of 0.09 A g^{-1} were applied to all cells to reach a Coulombic efficiency over 90% before the following tests. The reversible capacity correlated with the preparation condition. Figure 4c compiles the average size of Fe_3O_4 nanoparticles and the reversible capacity of all kinds of Fe_3O_4–SACNT composites at various speeds of film drawing. At the 20th cycle, Fe_3O_4–SACNT-2 and Fe_3O_4–SACNT-3 samples showed high specific capacities of 1461 and 1312 mAh g^{-1}, respectively, based on the mass of Fe_3O_4 (Figure 4c). In contrast, Fe_3O_4–SACNT-1 displayed a fast capacity fading and only delivered 919 mAh g^{-1} after 20 cycles (Figure S3). Even though Fe_3O_4–SACNT-6 also showed a high specific capacity of 1470 mAh g^{-1}, we did not take it into further consideration, as the mass fraction of Fe_3O_4 is less than 40%.

Therefore, the evaluation of cycling and rate capability of Fe_3O_4–SACNT composite anodes was narrowed to Fe_3O_4–SACNT-2 and Fe_3O_4–SACNT-3 samples with mass fractions of 50–60% and particle diameters of 5–7 nm. The characterization of cycling stability was performed at 0.1 A g^{-1} (Figure 5a) after the conditioning cycles (resulting in a kink in the figure). The first discharge/charge capacities of a Fe_3O_4–SACNT-2 sample in Figure 5a were 1814 mAh g^{-1} and 1117 mAh g^{-1}, respectively. The poor Coulombic efficiency of only 61.6% for the first cycle is ubiquitous for electrochemical reactions with lithium through a conversion reaction.[39] From the 10th cycle, the specific capacity kept increasing until the 80th cycle, at which a maximum was reached. We note that this increase may stem from a reversible nanogel formation on the Fe_3O_4 particles that has been observed and reported in similar systems.[40] After 80 cycles, the discharge capacity started to decrease, and a high specific capacity of 1670 mAh g^{-1} can still be delivered at the 100th cycle. The Coulombic efficiency increased to over 90% rapidly and then slowly increased to 95%, as shown in Figure 5a. In contrast to the Fe_3O_4–SACNT electrodes, a Fe_3O_4–Super P electrode made with the traditional slurry casting method only revealed a rapid capacity fading and a poor capacity of 200 mAh g^{-1} after 10 discharge/charge cycles (Figure S4).

dx.doi.org/10.1021/nl3046409 | *Nano Lett.* 2013, 13, 818–823

Since SACNTs account for ca. 50 wt % in Fe_3O_4–SACNT-2 and Fe_3O_4–SACNT-3 samples, it is more reasonable to reevaluate the specific capacity based on the total mass of the composite anodes. After such conversion, the specific capacity for the above Fe_3O_4–SACNT-2 sample can still reach 836 mAh g^{-1} after 100 cycles. This value far outperformed graphite. For high rate applications, the battery was discharged at 0.09 A g^{-1} but was charged at a variety of current densities with a stepwise manner. As shown in Figure 5b, the specific capacity for a Fe_3O_4–SACNT-3 sample can still reach 1250 mAh g^{-1} or 716 mAh g^{-1} based on the total mass of the electrode, as the charging current density increased to 0.9 A g^{-1}. The feature of capacity increasing disappeared at this current density. The reversible specific capacity was investigated at current densities up to 9 A g^{-1}, almost equivalent to 25 *C* of graphite electrodes (1*C* = 0.37 A g^{-1} for graphite). At this high current density, the Fe_3O_4–SACNT-3 sample can still deliver 340 mAh g^{-1}, or 194 mAh g^{-1} based on the total mass. What we should emphasize is the great reversibility and capacity retention. After such high current density test, the reversible capacity can still recover to 1550 mAh g^{-1} (or 885 mAh g^{-1}) at 0.09 A g^{-1} and 923 mAh g^{-1} (or 529 mAh g^{-1}) at 1.8 A g^{-1} based on the mass of Fe_3O_4 (or total mass). A rough comparison indicated that the reversible capacity obtained in the rate capability tests is better than previously reported data, such as graphene-wrapped Fe_3O_4 that only delivered 520 mAh g^{-1} at 1.75 A g^{-1}.[41] We note that all of the Fe_3O_4–SACNT-2 and Fe_3O_4–SACNT-3 samples performed almost equally and hence briefly summarize that the performance of Fe_3O_4–SACNT composite electrodes can be optimized by the condition of synthesis due to its strong correlation to the size of the Fe_3O_4 nanoparticles.

The excellent rate capability could be attributed to the nanosized Fe_3O_4 particles and low resistance benefited from SACNTs. The as-prepared Fe_3O_4–SACNT-2 and Fe_3O_4–SACNT-3 with 200-layer SACNT films displayed resistances of 27.3 Ω/sq and 26.8 Ω/sq, respectively. The postcycle values remained almost unchanged. Further insights as to the effect of SACNTs on the electrochemical performance can be gained from postcycle SEM and TEM images (Figure 5). There is no significant difference between precycle and postcycle SEM images at low magnifications (Figure 5c), revealing that the porous structure was highly preserved (Figure 5e). However, as shown in the TEM images, the microscopic morphology of Fe_3O_4 sheath was varied. In contrast to Figure 2d, the boundary between Fe_3O_4 particles after cycling was smeared out (Figure 5f). We attribute this observation of the structural change to the reduction of Fe_3O_4 into Fe and Li_2O in the lithiation process and the oxidation of Fe in the delithiation process. The thickness of the Fe_3O_4 sheath became slightly thicker in comparison with that of the precycle samples. Nevertheless, the porous structure and the flexibility of SACNTs would cushion this volumetric change. As a result, little cracks on Fe_3O_4 sheath were observed in the high magnification images (Figure 5f). Accordingly, the Fe_3O_4–CNT composite has exhibited advantages in reversible capacity, capacity retention, and rate capability for rechargeable LIBs.

Finally, the magnitudes of reversible specific capacity of Fe_3O_4–SACNT will be discussed. In theory, Fe_3O_4 can uptake 8 Li^+ per chemical formula and result in a reversible capacity of 924 mAh g^{-1}, as suggested in the following reaction equation,

$$Fe_3O_4 + 8Li^+ + 8e^- \leftrightarrow 4Li_2O + 3Fe$$

The Fe_3O_4–SACNT composite anodes always showed capacities higher than this theoretical value. One possibility is the contribution from the SACNT matrix. Chemically or mechanically modified CNTs were reported to have reversible capacities exceeding 1000 mAh g^{-1}.[42] However, after the Fe_3O_4 coating was dissolved in HCl, the bare SACNT only showed reversible capacities of 200 mAh g^{-1}, with good capacity retention for at least 80 cycles (Figure S5). The surface of SACNT may be affected by the collision of high energy sputtered atoms, but this mild functionalization is still incapable to remarkably enhance the reversible capacity of SACNT. Another possibility may lie in the interfacial Li storage in the nanomaterial. Extra storage capacity can be achieved by under potential deposition such as a Li monolayer bonded on the surface, reaction with electrolyte, or a charge separation at the SEI or phase boundaries.[43] These interfacial effects somehow disappeared when Fe_3O_4 was dissolved and therefore were not observed in the sole SACNT. Actually, the origin of extra storage capacity has been investigated both experimentally and theoretically.[44−46] The investigation and the utilization of interfacial storage in nanomaterial would be an interesting topic for the ongoing research.

In conclusion, we have integrated CNT film drawing and magnetron sputtering toward a one-step synthetic approach of Fe_3O_4–CNT composites. Electron microscopy studies reveal that this is a simple but effective fabrication method to achieve a uniform coating of metal oxides with controllable sizes and mass fractions. The ordered SACNT scaffold manifests itself as an excellent structure to host electrode materials for LIB applications. The free-standing Fe_3O_4–CNT composite is a promising anode material with superior specific capacities over 800 mAh g^{-1} based on the total electrode mass as well as excellent rate capabilities. The high overall specific capacity results from the removal of binder and metal current collectors. Furthermore, this sputtering synthesis can be expected to interface with available industrial production methods such as the roll-to-roll process in a large scale, and its potential applications to other transition metal oxides could be envisaged.

■ ASSOCIATED CONTENT

Supporting Information

Experimental detail; EDX spectrum of Fe_3O_4–SACNT; TEM image of pristine SACNT; galvanostatic results for Fe_3O_4–SACNT-1, Fe_3O_4–Super P and sputtered SACNT. This material is available free of charge via the Internet at http://pubs.acs.org.

■ AUTHOR INFORMATION

Corresponding Author

*E-mail: jpwang@tsinghua.edu.cn.

Notes

The authors declare no competing financial interest.

■ ACKNOWLEDGMENTS

The authors are grateful for financial support provided by the National Basic Research Program of China (2012CB932301), NSFC grants (51102146, 50825201, and 51102147), and the China Postdoctoral Science Foundation (2012M520261).

■ REFERENCES

(1) Armand, M.; Tarascon, J.-M. *Nature* **2008**, *451*, 652−657.

(2) Dunn, B.; Kamath, H.; Tarascon, J.-M. *Science* **2011**, *334*, 928−935.
(3) Thackeray, M. M.; Wolverton, C.; Isaacs, E. D. *Energy Environ. Sci.* **2012**, *5*, 7854.
(4) Hayner, C. M.; Zhao, X.; Kung, H. H. *Annu. Rev. Chem. Biomol. Eng.* **2012**, *3*, 445−471.
(5) Tarascon, J.-M.; Armand, M. *Nature* **2001**, *414*, 359−367.
(6) Winter, M.; Besenhard, J. O.; Spahr, M. E.; Novák, P. *Adv. Mater.* **1998**, *10*, 725−763.
(7) Chan, C. K.; Peng, H.; Liu, G.; McIlwrath, K.; Zhang, X. F.; Huggins, R. A.; Cui, Y. *Nat. Nanotechnol.* **2008**, *3*, 31−35.
(8) Cui, L.-F.; Ruffo, R.; Chan, C. K.; Peng, H.; Cui, Y. *Nano Lett.* **2009**, *9*, 491−495.
(9) Winter, M.; Besenhard, J. O. *Electrochim. Acta* **1999**, *45*, 31−50.
(10) Jiang, D.; Tian, H.; Qiu, C.; Ma, X.; Fu, Y. *J. Solid State Electrochem.* **2010**, *15*, 2639−2644.
(11) Kepler, K. D.; Vaughey, J. T.; Thackeray, M. M. *Electrochem. Solid-State Lett.* **1999**, *2*, 307−309.
(12) Huggins, R. A. *J. Power Sources* **1999**, *81*−*82*, 13−19.
(13) Wu, Z.-S.; Ren, W.; Wen, L.; Gao, L.; Zhao, J.; Chen, Z.; Zhou, G.; Li, F.; Cheng, H.-M. *ACS Nano* **2010**, *4*, 3187−3194.
(14) Reddy, A. L. M.; Shaijumon, M. M.; Gowda, S. R.; Ajayan, P. M. *Nano Lett.* **2009**, *9*, 1002−1006.
(15) Mornet, S.; Vasseur, S.; Grasset, F.; Duguet, E. *J. Mater. Chem.* **2004**, *14*, 2161−2175.
(16) Ho, D.; Sun, X.; Sun, S. *Acc. Chem. Res.* **2011**, *44*, 875−882.
(17) Zhang, Q.; Shi, Z.; Deng, Y.; Zheng, J.; Liu, G.; Chen, G. *J. Power Sources* **2012**, *197*, 305−309.
(18) Chen, Y.; Xia, H.; Lu, L.; Xue, J. *J. Mater. Chem.* **2012**, *22*, 5006.
(19) Duan, H.; Gnanaraj, J.; Chen, X.; Li, B.; Liang, J. *J. Power Sources* **2008**, *185*, 512−518.
(20) Taberna, P. L.; Mitra, S.; Poizot, P.; Simon, P.; Tarascon, J.-M. *Nat. Mater.* **2006**, *5*, 567−573.
(21) Lian, P.; Zhu, X.; Xiang, H.; Li, Z.; Yang, W.; Wang, H. *Electrochim. Acta* **2010**, *56*, 834−840.
(22) Ji, L.; Tan, Z.; Kuykendall, T. R.; Aloni, S.; Xun, S.; Lin, E.; Battaglia, V.; Zhang, Y. *Phys. Chem. Chem. Phys.* **2011**, *13*, 7170.
(23) Wang, L.; Yu, Y.; Chen, P. C.; Zhang, D. W.; Chen, C. H. *J. Power Sources* **2008**, *183*, 717−723.
(24) Ban, C.; Wu, Z.; Gillaspie, D. T.; Chen, L.; Yan, Y.; Blackburn, J. L.; Dillon, A. C. *Adv. Mater.* **2010**, *22*, E145−E149.
(25) Meunier, V.; Kephart, J.; Roland, C.; Bernholc, J. *Phys. Rev. Lett.* **2002**, *88*, 075506.
(26) Wu, Y. P.; Rahm, E.; Holze, R. *J. Power Sources* **2003**, *114*, 228−236.
(27) Bruce, P. G.; Scrosati, B.; Tarascon, J.-M. *Angew. Chem., Int. Ed.* **2008**, *47*, 2930−2946.
(28) Safi, I. *Surf. Coat. Technol.* **2000**, *127*, 203−219.
(29) Ziebert, C.; Ulrich, S. *J. Vac. Sci. Technol., A* **2006**, *24*, 554−583.
(30) Chen, Y.-M.; Cai, J.-H.; Huang, Y.-S.; Lee, K.-Y.; Tsai, D.-S.; Tiong, K.-K. *Thin Solid Films* **2012**, *520*, 2409−2413.
(31) Liu, C.-H.; Mao, B.-H.; Gao, J.; Zhang, S.; Gao, X.; Liu, Z.; Lee, S.-T.; Sun, X.-H.; Wang, S.-D. *Carbon* **2012**, *50*, 3008−3014.
(32) Jiang, K.; Li, Q.; Fan, S. *Nature* **2002**, *419*, 801−801.
(33) Jiang, K.; Wang, J.; Li, Q.; Liu, L.; Li, C.; Fan, S. *Adv. Mater.* **2011**, *23*, 1154−1161.
(34) Zhang, H.; Feng, C.; Zhai, Y.; Jiang, K.; Li, Q.; Fan, S. *Adv. Mater.* **2009**, *21*, 2299−2304.
(35) Wang, K.; Luo, S.; Wu, Y.; He, X.; Zhao, F.; Wang, J.; Jiang, K.; Fan, S. *Adv. Funct. Mater.* **2012**, DOI: 10.1002/adfm.201202412.
(36) Liu, H.; Jiang, E. Y.; Bai, H. L.; Zheng, R. K. *J. Appl. Phys.* **2004**, *95*, 5661−5665.
(37) Kanzaki, T.; Kitayama, K.; Shimokoshi, K. *J. Am. Ceram. Soc.* **1993**, *76*, 1491−1494.
(38) Naumkin, A. V.; Kraut-Vass, A.; Gaarenstroom, S. W.; Powell, C. J. *NIST Standard Reference Database 20*, Version 4.1 (web version); http://srdata.nist.gov/xps/, 2012.
(39) Cabana, J.; Monconduit, L.; Larcher, D.; Palacín, M. R. *Adv. Mater.* **2010**, *22*, E170−E192.
(40) Laruelle, S.; Grugeon, S.; Poizot, P.; Dollé, M.; Dupont, L.; Tarascon, J.-M. *J. Electrochem. Soc.* **2002**, *149*, A627−A634.
(41) Zhou, G.; Wang, D.-W.; Li, F.; Zhang, L.; Li, N.; Wu, Z.-S.; Wen, L.; Lu, G. Q. (Max); Cheng, H.-M. *Chem. Mater.* **2010**, *22*, 5306−5313.
(42) Gao, B.; Bower, C.; Lorentzen, J. D.; Fleming, L.; Kleinhammes, A.; Tang, X. P.; McNeil, L. E.; Wu, Y.; Zhou, O. *Chem. Phys. Lett.* **2000**, *327*, 69−75.
(43) Jamnik, J.; Maier, J. *Phys. Chem. Chem. Phys.* **2003**, *5*, 5215.
(44) Zhu, K.; Wang, Q.; Kim, J.-H.; Pesaran, A. A.; Frank, A. J. *J. Phys. Chem. C* **2012**, *116*, 11895−11899.
(45) Wang, Y.; Su, D.; Ung, A.; Ahn, J.; Wang, G. *Nanotechnology* **2012**, *23*, 055402.
(46) Zhukovskii, Y. F.; Balaya, P.; Kotomin, E. A.; Maier, J. *Phys. Rev. Lett.* **2006**, *96*, 058302.